Efficient frequency comb generation in AlGaAs-on-insulator

Pu, Minhao; Ottaviano, Luisa; Semenova, Elizaveta; Yvind, Kresten

Published in:
Optica

Link to article, DOI:
10.1364/OPTICA.3.000823

Publication date:
2016

Document Version
Publisher's PDF, also known as Version of record

optica

Efficient frequency comb generation in AlGaAs-on-insulator

Minhao Pu, Luisa Ottaviano, Elizaveta Semenova, and Kresten Yvind*

DTU Fotonik, Department of Photonics Engineering, Technical University of Denmark, Building 343, DK-2800 Kgs. Lyngby, Denmark
**Corresponding author: kryv@fotonik.dtu.dk*

Received 28 March 2016; revised 27 May 2016; accepted 20 June 2016 (Doc. ID 262016); published 26 July 2016

The combination of nonlinear and integrated photonics enables Kerr frequency comb generation in stable chip-based micro-resonators. Such a comb system will revolutionize applications, including multi-wavelength lasers, metrology, and spectroscopy. Aluminum gallium arsenide (AlGaAs) exhibits very high material nonlinearity and low nonlinear loss. However, difficulties in device processing and low device effective nonlinearity made Kerr frequency comb generation elusive. Here, we demonstrate AlGaAs-on-insulator as a nonlinear platform at telecom wavelengths with an ultra-high device nonlinearity. We show high-quality-factor ($Q > 10^5$) micro-resonators where optical parametric oscillations are achieved with milliwatt-level pump threshold powers, which paves the way for on-chip pumped comb generation.

OCIS codes: (190.4390) Nonlinear optics, integrated optics; (130.0130) Integrated optics; (230.7390) Waveguides, planar; (140.4780) Optical resonators; (190.3270) Kerr effect; (190.4970) Parametric oscillators and amplifiers.

http://dx.doi.org/10.1364/OPTICA.3.000823

Kerr effects enable various nonlinear applications, such as optical signal processing, metrology, spectroscopy, and quantum information science [1–4]. Desirable material properties for all-optical $\chi^{(3)}$ nonlinear chips are a high Kerr nonlinearity and low linear and nonlinear losses to enable high four-wave mixing (FWM) efficiency and parametric gain. Parametric oscillation and Kerr frequency comb generation have been first demonstrated on chips using silica toroidal resonators [5–7]. However, the delicate tapered-fiber coupling scheme makes it challenging for on-chip integration. Many planar integrated material platforms have been investigated, showing the different trade-offs between nonlinearity and losses [8–17], and Kerr frequency comb generations have also been realized in different platforms, including Hydex [9], Si_3N_4 [10,11], AlN [12], diamond [13], and silicon [17]. In addition to good intrinsic material properties, the ability to perform accurate and high-yield processing is desirable in order to integrate additional functionalities on the same chip and also to decrease linear losses. Silicon-on-insulator (SOI) is the model system for integration [4]. It supports a large index contrast and shallow etch depths, enabling patterning sub-micron structures with smooth sidewalls. However, due to two-photon absorption (TPA) at telecom wavelengths, e.g., 1550 nm, high parametric gain [16] and Kerr frequency comb generation [17] have only been achieved by pumping at wavelengths beyond 2000 nm. Therefore, an integrated nonlinear platform that combines a high material nonlinearity, a high-index contrast like SOI, and low linear and nonlinear losses is highly desirable.

Aluminum gallium arsenide ($Al_xGa_{1-x}A_s$) was identified early on as a promising candidate and even nominated as the "silicon of nonlinear optics" [18,19] when operated just below half its bandgap energy. It offers a high refractive index ($n \approx 3.3$) and a nonlinear index (n_2) [20–22] on the order of 10^{-17} m^2 W^{-1}, a large transparency window (from near- to mid-infrared), and the ability to engineer the material bandgap by varying the alloy composition (x) [22]. Its bandgap can be tailored in such a way that TPA, which is the main detrimental effect for the FWM process, is mitigated, and at the same time, the three-photon absorption is low [19] while a high material nonlinearity is maintained. Over the past two decades, efforts have been made to realize efficient nonlinear processes in AlGaAs waveguides [20–22]. However, the fabrication of such waveguides with very high and narrow mesa structures becomes very challenging and prevents advanced designs that go beyond simple straight waveguides. In addition, the low vertical index contrast of such waveguides limits the effective nonlinearity.

To enhance light confinement and relax the etching process requirements, we propose an AlGaAs-on-insulator (AlGaAsOI) platform, such as that shown in Fig. 1(a). In this layout, a thin $Al_xGa_{1-x}As$ layer on top of a low-index insulator layer resides on a semiconductor substrate. In this Letter, the aluminum fraction (x) is 17%, which makes the material bandgap 1.63 eV and the refractive index 3.33. Thanks to the large index contrast (~55%) of this layout, light can be confined in a sub-micron waveguide core. As the nonlinear parameter (γ) is highly dependent on the waveguide effective mode area (A_{eff}) as expressed by $\gamma = 2\pi n_2/\lambda A_{\text{eff}}$ [4], an ultra-high effective nonlinearity of ~660 W^{-1} m^{-1}, which is orders of magnitude higher than that of a typical Si_3N_4 waveguide [10,11], can be obtained for an AlGaAsOI waveguide using a cross-section dimension of 320 nm × 630 nm (see Supplement 1).

High index-contrast waveguide device performance is typically limited by linear losses induced by light scattering from surface roughness [17]. High-quality epitaxial material growth and substrate removal are required to ensure smoothness for the top and bottom

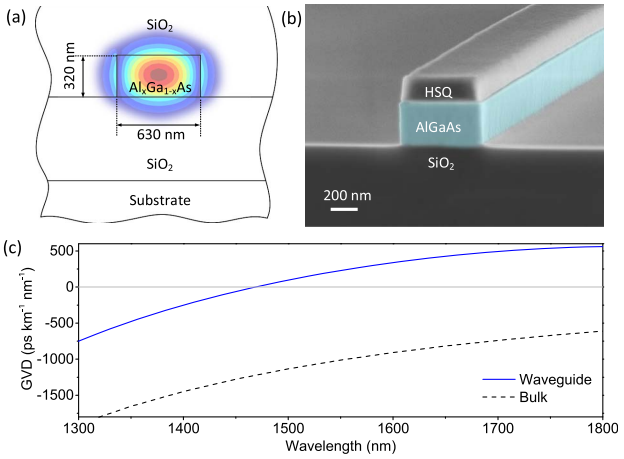

Fig. 1. AlGaAs-on-insulator (AlGaAsOI) nano-waveguide: (a) schematic drawing of an AlGaAsOI nano-waveguide with the simulated electric field distribution for the fundamental TE mode. (b) SEM picture of an AlGaAsOI nano-waveguide (highlighted in blue) after the dry etching process. (c) Calculated group velocity dispersion (GVD) versus wavelength for the waveguide with 320 nm × 630 nm cross-section dimensions. The dashed curve shows the GVD for the bulk AlGaAs material.

waveguide surfaces, while good lithography and dry etching processes define the waveguide sidewall surface roughness. The preparation of AlGaAsOI samples includes wafer growth, wafer bonding, and substrate removal (see Supplement 1). A 320-nm-thick layer of AlGaAs was grown in a low-pressure metalorganic vapor phase epitaxy reactor on a 50 mm GaAs (100) substrate with sacrificial layers consisting of InGaP and GaAs epi-layer stacks. After depositing a 3-μm-thick silica layer on the AlGaAs layer using plasma-enhanced chemical vapor deposition (PECVD), a 90-nm-thick benzocyclobutene layer was used as a bonding polymer between the grown wafer and another 50-mm semiconductor substrate (InP in this case) covered with a 10-nm-thick silica layer. The bonding process was performed under a partial vacuum ($\sim 3 \times 10^{-2}$ Pa) at 250°C for one hour in a wafer bonding system, while a force of 750 N was applied to the wafers. Subsequently, the GaAs substrate and the sacrificial layers were removed by wet etching. It is crucial to use the proper etch-stop layer and etchant, as the etching byproducts may result in roughness and absorption sites on the AlGaAs film surface (see Supplement 1). The sacrificial GaAs and InGaP layers were etched in a citric acid ($C_6H_8O_7$): hydrogen peroxide (H_2O_2) solution and hydrochloric (HCl) acid, respectively. Electron beam lithography (EBL, JEOL JBX-9500FS) was used to define the device pattern in the electron beam resist hydrogen silsesquioxane (HSQ, Dow Corning FOX-15). The device pattern was then transferred into the AlGaAs layer using a boron trichloride (BCl_3)-based dry etching process in an inductive coupled plasma reactive ion etching machine. As the refractive index of HSQ is relatively low (similar to SiO_2), it was kept on top of the AlGaAs device pattern. Finally, clad in a 3-μm-thick silica layer using PECVD, the chip was cleaved to form the input and output facets where nano-tapers enable efficient chip-to-fiber coupling for characterization [23]. Figure 1(b) shows a scanning electron microscope (SEM) picture of a fabricated AlGaAsOI waveguide with about 1.4 dB/cm linear loss.

In addition, the waveguide dispersion dominates over material dispersion for sub-wavelength-sized waveguides, and therefore, the group velocity dispersion can be engineered from the normal dispersion of bulk material to the anomalous dispersion that is required to achieve parametric gain in nonlinear processes [16]. Figure 1(c) shows the waveguide dispersion calculated using the finite-element method mode solver in COMSOL for the transverse electric (TE) mode in the wavelength range between 1300 and 1800 nm. The Sellmeier equation was used to incorporate the dispersion of SiO_2, and the modified single effective oscillator model was used for AlGaAs [24].

Combining the ultra-high effective nonlinearity and low loss, AlGaAsOI can be used for ultra-efficient nonlinear parametric processes, such as low-threshold Kerr frequency comb generation, once a high-quality-factor (Q) micro-resonator is realized. To get a smooth pattern definition for bent waveguides in micro-resonators, a multi-pass exposure was applied to mitigate the stitching between pattern segments fractured during the EBL (see Supplement 1). Figure 2(a) shows an SEM picture of an 810-μm-long race track-shaped AlGaAsOI micro-resonator. Figure 2(b) shows a coupling gap of 170 nm for the resonator where the light propagating in the 450-nm-wide bus waveguide can be evanescently coupled to the 630-nm-wide curved (17.5 μm radius) waveguide of the resonator. Figure 2(c) shows the measured transmission spectrum for the resonance at 1589.64 nm for the TE mode, and the measured linewidth is around 9.6 pm, which corresponds to a loaded Q of ~165, 600. The measured loaded Q for all the devices ranges from 1.5×10^5 to 2.0×10^5, which is more than an order of magnitude higher than previously demonstrated Q for AlGaAs micro-ring resonators [25]. The resonator works in the under-coupled regime, and its transmission over a 10 nm wavelength range is shown in Fig. 2(d). Only one mode family with a free spectral range (FSR) of ~0.82 nm (98 GHz) is observed in the spectrum, which implies that the resonator waveguide with anomalous dispersion can be operated in a single-mode state. Therefore, the dispersion distortion

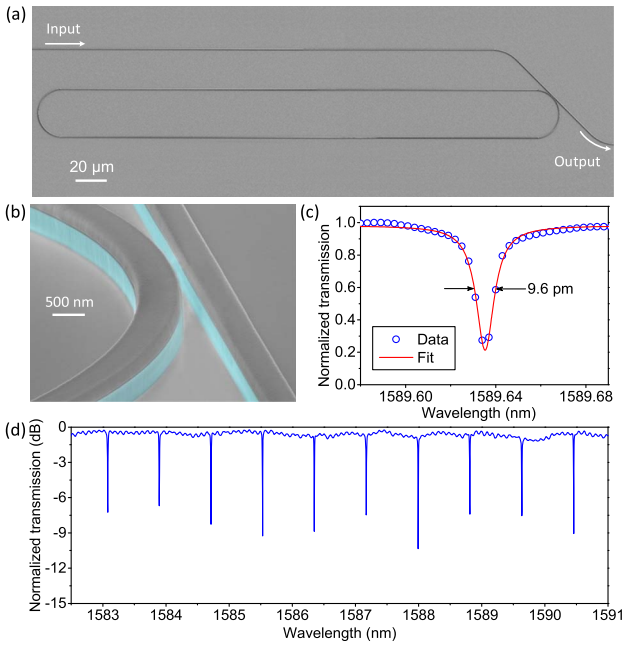

Fig. 2. (a) Top-view SEM image of the AlGaAsOI micro-resonator showing ring and bus waveguides. (b) Isometric-view SEM image of the coupling region of the AlGaAsOI micro-resonator where the AlGaAs material is indicated in blue. Measured (normalized) transmission spectrum of the AlGaAsOI micro-resonator (c) around the resonance at 1590 nm with a loaded quality factor (Q) of ~165, 600 and (d) over a 10 nm wavelength range.

induced by the inter-mode interaction between different mode families can be completely avoided, which is preferable for Kerr frequency comb generation (especially temporal soliton formation [26]) but not attainable in all nonlinear material platforms.

Kerr frequency comb generation is based on optical parametric oscillation (OPO), which relies on a combination of parametric amplification and oscillation as a result of the nonlinear FWM processes within the micro-resonator. As a continuous-wave pump light is tuned into a cavity resonance to achieve thermal soft locking [27], the built-up intra-cavity power triggers OPO at a critical power threshold when the round-trip parametric gain exceeds the round-trip loss of the resonator. To satisfy the momentum conservation in the FWM process, the pump energy can only be transferred to equispaced frequencies within the supported resonances of the micro-resonator [1] and thus forms a frequency comb at the output, as illustrated in Fig. 3(a). The measured spectrum of an AlGaAsOI micro-resonator is shown in Fig. 3(b) when a pump power of 72 mW was coupled into the bus waveguide. A frequency comb with the native line spacing (single FSR) spanning over about 350 nm was observed. To further increase the comb bandwidth, the waveguide dimension can be optimized to get a low and flat anomalous dispersion [28].

The threshold power in the bus waveguide can be estimated by the expression [29] $P_{\mathrm{th}} \approx 1.54(\frac{\pi}{2})\frac{Q_C}{2Q_L}\frac{n^2 L A_{\mathrm{eff}}}{n_2 \lambda_P}\frac{1}{Q_L^2}$, where L and λ_p, are the cavity length and pump wavelength, and Q_C and Q_L are the coupling and loaded quality factors of the micro-resonator, respectively. As Q_L and L are correlated, we measured the threshold power for resonators with different cavity lengths (FSR ranging from 98 to 995 GHz) to find their influences on the threshold power. The obtained minimum threshold power was 3 mW for a micro-ring resonator [see Fig. 4(a)] with a Q_L of about 10^5. The output power of the primary OPO sideband increases significantly at threshold, as shown in Fig. 4(b). Figure 4(c) shows the measured output spectrum for this resonator with a pump power (4.5 mW) slightly above the threshold. It shows a typical OPO initial state in which widely spaced (multi-FSR spacing) primary sidebands are generated [30]. The measured threshold power for different devices as a function of Q_L is shown in Fig. 4(d), where most of the resonators are seen to have milliwatt-level thresholds, although resonators with a smaller FSR exhibit a slightly higher threshold. The measured data follows the theoretically predicted threshold trend, as shown by the colored bands.

As the dynamics of Kerr frequency comb generation have been extensively studied [26–33] and mode-locked combs have been demonstrated [32,33], Kerr frequency comb technologies are approaching practical applications. Table 1 summarizes several material platforms where frequency comb generation has been demonstrated on chips at telecom wavelengths. Here we focus on chip systems, therefore, CaF_2 and MgF_2 crystalline resonators [27,31] are not included, though high-performance combs have been reported. For a compact chip-sized comb system, planar integrated platforms are of critical importance because of their robust coupling scheme and potential to be integrated with on-chip light sources. A low threshold is crucial for the realization of such a system. As shown in Table 1, the linear refractive index of AlGaAs is the highest among these platforms, which makes it the most suitable platform for compact circuits. In addition, the material nonlinear index of AlGaAs is orders of magnitude larger than those of the other platforms. These intrinsic material properties make AlGaAsOI an ultra-efficient platform for nonlinear parametric processes. Therefore, even though the Q_L of our device is still relatively low, the threshold powers for the AlGaAsOI micro-resonators with FSR (or repetition rate) in the hundreds-of-gigahertz range are all within the milliwatt level. For some important applications, such as self-referencing, the repetition rates need to be within a detectable range of fast photodiodes (<100 GHz). At our current linear loss level, the threshold

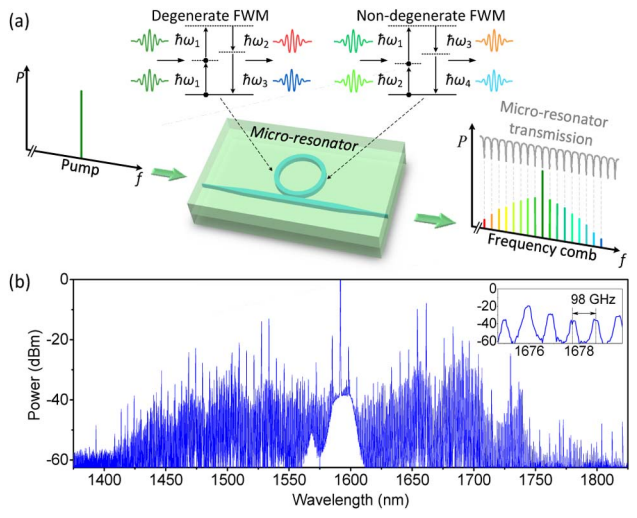

Fig. 3. Optical frequency comb generation in an AlGaAsOI micro-resonator: (a) a single-frequency pump light coupled into a high-Q micro-resonator enables efficient parametric processes [degenerate and non-degenerate four-wave mixing (FWM)] in the resonator and allows new frequency generation in the supported modes of the micro-resonator. (b) The output spectrum of an 810-μm-long AlGaAsOI micro-resonator when a 72-mW pump was coupled into the resonator at ~1590 nm. A frequency comb was generated with a line spacing of 98 GHz over a wavelength range of about 350 nm.

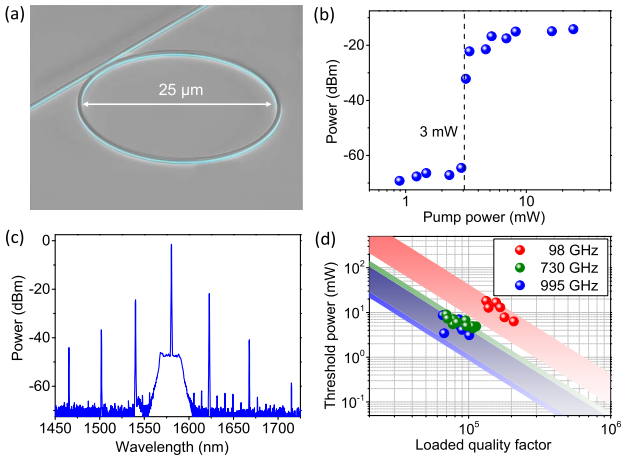

Fig. 4. OPO threshold measurement: (a) isometric view SEM image of a 25-μm-diameter AlGaAsOI micro-resonator with a FSR of 995 GHz. (b) Measured primary sideband power at the chip output as a function of pump power in the bus waveguide for the resonator shown in (a). A significant power increase was observed at the threshold of 3.1 mW. (c) The output spectrum of the OPO when the pump power was increased to just above the threshold power (4.5 mW) for the same micro-resonator in (a). (d) The measured threshold power for micro-resonators with three different FSRs: 98, 730, and 995 GHz. The colored bands show the theoretical threshold power ranges for the different micro-resonators (from critical-coupling with $Q_C = 2Q_L$ to under-coupling with $Q_C = 10Q_L$).

Table 1. Comparison of Nonlinear Platforms for On-Chip Frequency Comb Generation at Telecom Wavelengths

Material Platform	n	n_2 (m^2/W)	Waveguiding Area (μm^2)	FSR (GHz)	Q	P_{th} (mW)	Coupling Waveguide[a]
Silica [7]	1.4	2.2×10^{-20}	30[b]	33	2.7×10^8	1	Tapered fiber
Hydex [9]	1.7	1.2×10^{-19}	1.45×1.50	200	1×10^6	50	Integrated
Si_3N_4 [11]	2.0	2.5×10^{-19}	0.60×3.00	25	1.7×10^7	5	Integrated
AlN [12]	2.1	2.3×10^{-19}	0.65×3.50	435	8×10^5	200	Integrated
Diamond [13]	2.4	8.2×10^{-20}	0.95×0.85	925	1×10^6	20	Integrated
$Al_{0.17}Ga_{0.83}As$ (this work)	3.3	2.6×10^{-17}	0.32×0.62	995/98	$1 \times 10^5/2 \times 10^5$	3/6	Integrated

[a]Configuration of bus waveguide coupling to the resonator.
[b]Effective area for the wedge micro-resonator.

power will be above the single-digit milliwatt level if the FSR is less than 50 GHz, since the Q_L saturates at approximately 2×10^5 as the cavity length is further increased (see Supplement 1). A Q_L of 4×10^5 is required to obtain a milliwatt (sub-milliwatt) -level threshold for a 15 GHz (200 GHz) resonator. With the optimization of the fabrication processes and waveguide and resonator designs (see Supplement 1), AlGaAsOI devices with a higher Q can be fabricated. In line with the fast-growing hybrid integration trend to combine different materials in multiple levels on a single CMOS-compatible chip, the AlGaAsOI platform is very promising for realizing a fully integrated comb system.

Because of the wide transparency window of AlGaAs materials, the frequency comb can potentially be extended into the mid-infrared with proper dispersion engineering (see Supplement 1). Besides comb generation, we have recently demonstrated wavelength conversion of a serial data signal at a record high speed (beyond terabaud) in this platform [34]. An ultra-broad bandwidth and ultra-high efficiency make AlGaAsOI an excellent platform for optical signal processing in telecommunications. Moreover, AlGaAs exhibits strong $\chi^{(2)}$ effects [35] due to its non-centrosymmetric crystal structure. Therefore, the AlGaAsOI platform is also suitable for combining both $\chi^{(2)}$ and $\chi^{(3)}$ effects to obtain, for example, multi-octave spanning combs [36].

Funding. Teknologi og Produktion, Det Frie Forskningsråd (FTP 11-117031); Villum Fonden Centre of Foundation (NATEC).

Acknowledgment. We thank Jan W. Thomsen at Copenhagen University, Christophe Peucheret at Université de Rennes 1, Molly Piels, Hao Hu, Leif K. Oxenløwe, and Jesper Mørk at the Technical University of Denmark for the motivating and helpful discussions and comments on this Letter.

See Supplement 1 for supporting content.

REFERENCES

1. T. J. Kippenberg, R. Holzwarth, and S. A. Diddams, Science **332**, 555 (2011).
2. T. Udem, R. Holzwarth, and T. W. Hänsch, Nature **416**, 233 (2002).
3. A. Schliesser, N. Picque, and T. W. Hänsch, Nat. Photonics **6**, 440 (2012).
4. J. Leuthold, C. Koos, and W. Freude, Nat. Photonics **4**, 535 (2010).
5. T. J. Kippenberg, S. M. Spillane, and K. J. Vahala, Phys. Rev. Lett. **93**, 083904 (2004).
6. P. Del'Haye, A. Schliesser, O. Arcizet, T. Wilken, R. Holzwarth, and T. J. Kippenberg, Nature **450**, 1214 (2007).
7. J. Li, H. Lee, T. Chen, and K. J. Vahala, Phys. Rev. Lett. **109**, 233901 (2012).
8. B. J. Eggleton, B. Luther-Davies, and K. Richardson, Nat. Photonics **5**, 141 (2011).
9. L. Razzari, D. Duchesne, M. Ferrera, R. Morandotti, S. Chu, B. E. Little, and D. J. Moss, Nat. Photonics **4**, 41 (2010).
10. J. S. Levy, A. Gondarenkon, M. A. Foster, A. C. Turner-Foster, A. L. Gaeta, and M. Lipson, Nat. Photonics **4**, 37 (2010).
11. Y. Xuan, Y. Liu, X. Xue, P. Wang, J. Wang, B. Niu, K. Han, M. Teng, D. E. Leaird, A. M. Weiner, and M. Qi, in *Conference on Lasers and Electro-Optics*, OSA Technical Digest (online) (Optical Society of America, 2015), paper STu1I.6.
12. H. Jung, C. Xiong, K. Y. Fong, X. Zhang, and H. X. Tang, Opt. Lett. **38**, 2810 (2013).
13. B. J. M. Hausmann, I. Bulu, V. Venkataraman, P. Deotare, and M. Loncar, Nat. Photonics **8**, 369 (2014).
14. B. Kuyken, H. Ji, S. Clemmen, S. K. Selvaraja, H. Hu, M. Galili, P. Jeppesen, G. Morthier, S. Massar, L. K. Oxenløwe, G. Roelkens, and R. Baets, Opt. Express **19**, B146 (2011).
15. U. D. Dave, B. Kuyken, F. Leo, S. Gorza, S. Combrie, A. D. Rossi, F. Raineri, and G. Roelkens, Opt. Express **23**, 4650 (2015).
16. X. Liu, R. M. Osgood, Y. A. Vlasov, and W. M. J. Green, Nat. Photonics **4**, 557 (2010).
17. A. G. Griffith, R. K. W. Lau, J. Cardenas, Y. Okawachi, A. Mohanty, R. Fain, Y. H. D. Lee, M. Yu, C. T. Phare, C. B. Poitras, A. L. Gaeta, and M. Lipson, Nat. Commun. **6**, 6299 (2015).
18. G. I. Stegeman, A. Villeneuve, and J. Kang, Int. J. Nonlinear Opt. Phys. **3**, 347 (1994).
19. J. S. Aitchison, D. C. Hutchings, J. U. Kang, G. I. Stegeman, and A. Villeneuve, IEEE J. Quantum. Electron. **33**, 341 (1997).
20. K. Dolgaleva, W. C. Ng, L. Qian, and J. I. Aitchison, Opt. Express **19**, 12440 (2011).
21. C. Lacava, V. Pusino, P. Minzioni, M. Sorel, and I. Cristiani, Opt. Express **22**, 5291 (2014).
22. J. J. Wathen, P. Apiratikul, C. J. K. Richardson, G. A. Porkolab, G. M. Carter, and T. E. Murphy, Opt. Lett. **39**, 3161 (2014).
23. M. Pu, L. Liu, H. Ou, K. Yvind, and J. M. Hvam, Opt. Commun. **283**, 3678 (2010).
24. M. A. Afromowitz, Solid State Commun. **15**, 59 (1974).
25. P. Kultavewuti, V. Pusino, M. Sorel, and J. S. Aitchison, Opt. Lett. **40**, 3029 (2015).
26. T. Herr, V. Brasch, J. D. Jost, I. Mirgorodskiy, G. Lihachev, M. L. Gorodetsky, and T. J. Kippenberg, Phys. Rev. Lett. **113**, 123901 (2014).
27. I. S. Grudinin, N. Yu, and L. Maleki, Opt. Lett. **34**, 878 (2009).
28. Y. Okawachi, K. Saha, J. S. Levy, Y. H. Wen, M. Lipson, and A. L. Gaeta, Opt. Lett. **36**, 3398 (2011).
29. A. B. Matsko, A. A. Savchenkov, D. Strekalov, V. S. Ilchenko, and L. Maleki, Physica Rev. A **71**, 033804 (2005).
30. T. Herr, K. Hartinger, J. Riemensberger, C. Y. Wang, E. Gavartin, R. Holzwarth, M. L. Gorodetsky, and T. J. Kippenberg, Nat. Photonics **6**, 480 (2012).
31. W. Liang, A. A. Savchenkov, A. B. Matsko, D. Seidel, and L. Maleki, Opt. Lett. **36**, 2290 (2011).
32. T. Herr, V. Brasch, J. D. Jost, C. Y. Wang, N. M. Kondratiev, M. L. Gorodetsky, and T. J. Kippenberg, Nat. Photonics **8**, 145 (2014).
33. X. Xue, Y. Xuan, Y. Liu, P. Wang, S. Chen, J. Wang, D. E. Leaird, M. Qi, and A. M. Weiner, Nat. Photonics **9**, 594 (2015).
34. M. Pu, H. Hu, L. Ottaviano, E. Semenova, D. Vukovic, L. K. Oxenløwe, and K. Yvind, in *Optical Fiber Communication Conference Post Deadline Papers*, OSA Technical Digest (online) (Optical Society of America, 2015), paper Th5A.3.
35. S. Mariani, A. Andronico, A. Lemaitre, I. Favero, S. Ducci, and G. Leo, Opt. Lett. **39**, 3062 (2014).
36. H. Jung, R. Stoll, X. Guo, D. Fischer, and H. X. Tang, Optica **1**, 396 (2014).